J Therm Anal Calorim (2013) 114:205–212
DOI 10.1007/s10973-012-2927-9

Preparation of magnetic nanocrystalline $Mn_{0.5}Mg_{0.5}Fe_2O_4$ and kinetics of thermal decomposition of precursor

Kaiwen Zhou · Wenwei Wu · Yongni Li · Xuehang Wu · Sen Liao

Received: 12 October 2012 / Accepted: 20 December 2012 / Published online: 20 January 2013

Abstract The spinel $Mn_{0.5}Mg_{0.5}Fe_2O_4$ was obtained via calcining $Mn_{0.5}Mg_{0.5}Fe_2(C_2O_4)_3{\cdot}5H_2O$ above 400 °C in air. The precursor and its calcined products were characterized by thermogravimetry and differential scanning calorimetry, Fourier transform FT-IR, X-ray powder diffraction, scanning electron microscopy, energy dispersive X-ray spectrometer, and vibrating sample magnetometer. The results showed that $Mn_{0.5}Mg_{0.5}Fe_2O_4$ obtained at 600 °C had a specific saturation magnetization of 46.2 emu g^{-1}. The thermal decomposition of $Mn_{0.5}Mg_{0.5}Fe_2(C_2O_4)_3{\cdot}5H_2O$ below 450 °C experienced two steps which involved, at first, the dehydration of five water molecules and then decomposition of $Mn_{0.5}Mg_{0.5}Fe_2(C_2O_4)_3$ into spinel $Mn_{0.5}Mg_{0.5}Fe_2O_4$ in air. Based on Starink equation, the values of the activation energies associated with the thermal decomposition of $Mn_{0.5}Mg_{0.5}Fe_2(C_2O_4)_3{\cdot}5H_2O$ were determined.

Keywords Nanoparticles · Ferrites · Chemical synthesis · Non-isothermal kinetics · Thermal process

Introduction

Spinels of the type $M^{2+}M_2^{3+}O_4$ are always the focus of attention due to their versatility [1–3]. In the case of M^{3+}=Fe^{3+}, the resulting spinel ferrites having a general chemical composition of MFe_2O_4 (*M*=Cu, Mn, Mg, Zn, Ni, Co, Ca, etc.) are widely used in the field of high-density information storage, magnetic separation, ferrofluids, catalysts, drug targeting, magnetic resonance imaging, and gas sensor [4–14]. The structure of ferrospinels depends on the outer electron configuration and radius of divalent cation, and distribution of cations at the different sites. For example, $ZnFe_2O_4$ is a kind of normal spinel ferrite, $NiFe_2O_4$ and $CoFe_2O_4$ are inverse spinels, and $MnFe_2O_4$ and MnZn ferrites are random spinel. The magnetic moment direction of cations in tetrahedral A-site is opposite with that in octahedral B-site. Therefore, magnetic moment of spinel ferrites can be regulated by distribution of different divalent cations at the different sites.

Nanosized $MnFe_2O_4$ is one of the most important magnetic materials. Its properties, such as magnetic behavior and gas-sensing properties, etc., are highly dependent on the synthesis method and doping elements. In recent years, different kinds of $MnFe_2O_4$ nanostructured materials have been successfully synthesized, such as nanoparticles [15–17], nanorods [18, 19], and nanofibers [20]. A TEA-assisted route was normally used to obtain the octahedral-like $MnFe_2O_4$ crystallites [21].

The doped manganese ferrite can improve its performance. Therefore, doped manganese ferrite caused great concern, and some progress has been made. It was reported that substitutions of Mn^{2+} with divalent cation led to improved magnetic properties of nanocrystalline ferrites [11, 22–29]. For example, when Mn^{2+} ions in spinel $MnFe_2O_4$ were partially substituted by Co^{2+} ions, $Co_{0.35}Mn_{0.65}Fe_2O_4$ obtained at 700 °C showed a specific saturation magnetization of 71.6 emu g^{-1} [11]. Rajesh et al. [22] synthesized $Mn_{1-x}Zn_xFe_2O_4$ ($x = 0.0$, 0.1, 0.3, 0.5, 0.6, 0.7, 0.9) by co-precipitation technique, and studied

Electronic supplementary material The online version of this article (doi:10.1007/s10973-012-2927-9) contains supplementary material, which is available to authorized users.

K. Zhou · W. Wu (✉) · Y. Li · X. Wu · S. Liao
School of Chemistry and Chemical Engineering, Guangxi University, Nanning 530004, People's Republic of China
e-mail: gxuwuwenwei@yahoo.com.cn

K. Zhou
School of Materials Science and Engineering, Guangxi University, Nanning 530004, People's Republic of China

their magnetic properties. The results showed that the specific saturation magnetization of $Mn_{1-x}Zn_xFe_2O_4$ and Curie temperature (T_C) decreased with increasing zinc content in $Mn_{1-x}Zn_xFe_2O_4$. Okasha [27] prepared $Mg_xMn_{1-x}Fe_2O_4$ (x = 0.0, 0.15, and 0.25) by γ-irradiation. The results showed that the specific saturation magnetization of $Mg_xMn_{1-x}Fe_2O_4$ increased after γ-irradiation, and remanent magnetization decreased after γ-irradiation. However, synthesis research of doped $MnFe_2O_4$ still has fewer reports in comparison with that of $MnFe_2O_4$. Therefore, new synthesis methods for $Mn_{1-x}M_xFe_2O_4$ (M = transition metals or alkaline-earth metals) still need to be studied and innovated further. Besides, the kinetics study of thermal decomposition for $Mn_{1-x}M_xFe_2O_4$ precursor is important to obtain high-quality crystalline doped $MnFe_2O_4$ for practical applications.

The aim of this study is to prepare polycrystalline $Mn_{0.5}Mg_{0.5}Fe_2O_4$ using $MnSO_4{\cdot}H_2O$, $MgSO_4{\cdot}7H_2O$, $FeSO_4{\cdot}7H_2O$, and $Na_2C_2O_4$ as raw materials via solid-state reaction at low heating temperatures [6, 11] and to study magnetic properties of $Mn_{0.5}Mg_{0.5}Fe_2O_4$, the mechanisms, and kinetics of thermal decomposition of precursor. The kinetics of thermal decomposition of precursor was studied using TG/DTG/DSC techniques. Non-isothermal kinetics of thermal decomposition of precursor was interpreted by Starink equation [30, 31]. The kinetic parameters (E_a, A, mechanism) of thermal decomposition of $Mn_{0.5}Mg_{0.5}Fe_2(C_2O_4)_3{\cdot}5H_2O$ were discussed for the first time.

Experimental

Reagent and apparatus

All chemicals were of reagent-grade purity (<99.9 %). TG/DSC measurements were taken using a Netzsch Sta 409 PC/PG thermogravimetric analyzer and sample mass was around 11 mg. In order to make ferrous oxalate in the precursor decomposition into Fe_2O_3 during the heating, and then Fe_2O_3 reaction with MgO and MnO into $Mn_{0.5}Mg_{0.5}Fe_2O_4$, a continuous flow of air (40 mL min^{-1}) was passed into the reaction chamber. The reference material for DSC was Al_2O_3. X-ray powder diffraction (XRD) was performed using a Rigaku D/max 2,500 V diffractometer equipped with a graphite monochromator and a Cu target. The radiation applied was CuK_α ($\lambda = 0.15406$ nm), operating at 40 kV and 50 mA. XRD scans were made from 5° to 70° in 2θ with steps of 0.016°. Fourier transform FT-IR spectra of the precursor and its calcined products were recorded on a Nexus 470 Fourier transform FT-IR instrument in KBr pellets in the range of 4,000–400 cm^{-1}. The morphologies of the calcined samples and energy dispersive X-ray spectrometer (EDS) were obtained on S-3400 scanning electron microscopy (SEM). The specific magnetization (Ms) of the calcined sample powder was carried out at room temperature using a magnetic property measurement system (SQUID-MPMS-XL-5).

Preparation of $Mn_{0.5}Mg_{0.5}Fe_2O_4$

The $Mn_{0.5}Mg_{0.5}Fe_2O_4$ precursor was prepared by solid-state reaction at low heating temperatures using $MnSO_4{\cdot}H_2O$, $MgSO_4{\cdot}7H_2O$, $FeSO_4{\cdot}7H_2O$, and $Na_2C_2O_4$ as raw materials at first [3]. In a typical synthesis, $MnSO_4{\cdot}H_2O$ (8.36 g), $MgSO_4{\cdot}7H_2O$ (12.19 g), $FeSO_4{\cdot}7H_2O$ (55.00 g), $Na_2C_2O_4$ (41.57 g), and surfactant polyethylene glycol (PEG)-400 (3.5 mL, 50 vol.%) were put in a mortar, and the mixture was fully ground by hand with a rubbing mallet for 35 min. The grinding velocity was about 220 circles min^{-1}, and the strength applied was moderate. The reactant mixture gradually became damp, and then a paste formed quickly. The reaction mixture was kept at room temperature for 2 h. The mixture was washed with deionized water to remove soluble inorganic salts until SO_4^{2-} ion could not be visually detected with a 0.5 mol L^{-1} $BaCl_2$ solution. The solid was then washed with a small amount of anhydrous ethanol and dried at 75 °C for 6 h. The resulting material was subsequently determined to be $Mn_{0.5}Mg_{0.5}Fe_2(C_2O_4)_3{\cdot}5H_2O$. Nanocrystalline $Mn_{0.5}Mg_{0.5}Fe_2O_4$ with cubic structure was obtained via calcining $Mn_{0.5}Mg_{0.5}Fe_2(C_2O_4)_3{\cdot}5H_2O$ above 400 °C in air.

Method of determining kinetic parameters, and mechanism functions

Determination of activation energy by Starink equation

Activation energy of thermal decomposition of solid compound can be obtained by Starink equation (Eq. 1).

$$\ln\left(\frac{\beta_i}{T_{\alpha,i}^{1.92}}\right) = \text{Const} - 1.0008\left(\frac{E_\alpha}{RT_\alpha}\right), \quad (1)$$

where β_i is the heating rate (K min^{-1}), T_α is the reaction temperature (K) corresponding to degree of conversion (α) in TG curve, E_α is the activation energy (kJ mol^{-1}) of thermal decomposition corresponding to degree of conversion (α), R is the gas constant (8.314×10^{-3} kJ mol^{-1} K^{-1}). The dependence of $\ln\left(\beta_i/T_{\alpha,i}^{1.92}\right)$ on $1/T_\alpha$ must give rise to a straight line. Thus, reaction activation energy E_α can be obtained from linear slope ($-1.0008\ E_\alpha/R$, Eq. 1).

Determination of most probable mechanism functions

The following equation was used to estimate the most correct reaction mechanism of thermal decomposition of $Mn_{0.5}Mg_{0.5}Fe_2(C_2O_4)_3{\cdot}5H_2O$, i.e., $g(\alpha)$ function [32, 33]:

$$\ln g(\alpha) = \left[\ln\frac{AE_a}{R} + \ln\frac{e^{-x}}{x^2} + \ln h(x)\right] - \ln\beta, \quad (2)$$

where $x = E_a/(RT)$, $h(x) = \frac{x^4+18x^3+86x^2+96x}{x^4+20x^3+120x^2+240x+120}$, and β is the heating rate (K min^{-1}). The conversions α corresponding to multiple rates at the same temperature are put into the left of Eq. (2), combined with 31 types of mechanism functions [33, 34], the slope k and correlation coefficient r^2 are obtained from the plot of ln $g(\alpha)$ versus ln β. The probable mechanism function is the one for which the value of the slope k is near –1.00000 and correlation coefficient r^2 is better.

Calculation of pre-exponential factor *A*

The pre-exponential factor was estimated from Eq. (3) [31]:

$$A = \frac{\beta g(\alpha) E_\alpha}{RT_{max}^2}\exp\left(\frac{E_\alpha}{RT_{max}}\right) \quad (3)$$

where A is the pre-exponential factor (s^{-1}), β is the heating rate (K min^{-1}), $g(\alpha)$ is the most probably mechanism function determined by Eq. (2), E_α is the activation energy (kJ mol^{-1}) of thermal decomposition, R is the gas constant (8.314×10^{-3} kJ mol^{-1} K^{-1}), and T_{max} is the most rapid decomposition temperature (i.e., peak temperature in DTG curve, K).

Results and discussion

TG/DTG/DSC analysis of the precursor

Figure 1 shows the TG/DTG/DSC curves of $Mn_{0.5}Mg_{0.5}Fe_2(C_2O_4)_3{\cdot}5H_2O$ at four heating rates of 5, 10, 15, and 20 K min^{-1} in air.

The TG/DTG/DSC curves show that thermal decomposition of the $Mn_{0.5}Mg_{0.5}Fe(C_2O_4)_3{\cdot}5H_2O$ below 450 °C occured in two well-defined steps. For heating rate of 10 K min^{-1}, the first step starts at 40 °C, ends at 205 °C, and is characterized by a weak DTG peak at about 201 °C and a strong endothermic DSC peak at 207 °C, which can be attributed to dehydration of the five crystal water molecules from $Mn_{0.5}Mg_{0.5}Fe_2(C_2O_4)_3{\cdot}5H_2O$ (mass loss: observed, 17.82 %; theo., 17.82 %). The second decomposition step begins at 205 °C, ends at 449 °C, and is characterized by a strong DTG peak at 230 °C and a strong DSC exothermic peak at 266 °C, attributed to decomposition of $Mn_{0.5}Mg_{0.5}Fe_2(C_2O_4)_3$ into cubic $Mn_{0.5}Mg_{0.5}Fe_2O_4$ in air by one step, and of six CO_2 (mass loss: observed, 39.39 %; theo., 39.57 %). No other exothermic DSC peak that was ascribed to crystallization of $Mn_{0.5}Mg_{0.5}Fe_2O_4$ below 450 °C except exothermic DSC peak at 266 °C, which indicated that exothermic DSC peak of crystallization of $Mn_{0.5}Mg_{0.5}Fe_2O_4$ was overlapped with exothermic DSC peak from decomposition of $Mn_{0.5}Mg_{0.5}Fe_2(C_2O_4)_3$ in air. In other words, The decomposition of $Mn_{0.5}Mg_{0.5}Fe_2(C_2O_4)_3$ and crystallization of cubic $Mn_{0.5}Mg_{0.5}Fe_2O_4$ were almost finished at the same temperature. Crystalline $Mn_{0.5}Mg_{0.5}Fe_2O_4$ can be obtained at lower calcination temperature, which was attributed to Mn^{2+}, Mg^{2+}, and Fe^{2+} oxalates that have similar lower decomposition temperature, and ultra-fine the oxide particles with high activity formed by thermal decomposition of $Mn_{0.5}Mg_{0.5}Fe_2(C_2O_4)_3{\cdot}5H_2O$ can be easily in situ self-assembled into crystalline $Mn_{0.5}Mg_{0.5}Fe_2O_4$.

IR spectroscopic analysis of $Mn_{0.5}Mg_{0.5}Fe_2(C_2O_4)_3{\cdot}5H_2O$ and its calcined samples

The FT-IR spectra of $Mn_{0.5}Mg_{0.5}Fe_2(C_2O_4)_3{\cdot}5H_2O$ and its calcined sample are shown in Figure 2. The $Mn_{0.5}Mg_{0.5}Fe_2(C_2O_4)_3{\cdot}5H_2O$ exhibited a strong and broad band at about 3,373 cm^{-1}, which can be assigned to the stretching OH vibration of the water molecule. The strong band, which appeared at 1,653 cm^{-1} in the spectrum of the precursor, can be ascribed to the bending mode of the HOH [3, 6, 35–38]. The weak band at about 828 cm^{-1} was the water libration (hindered rotation). The band at 1,322 cm^{-1} can be assigned to either the appearance of new M-OC_2O_3 (M=Mn, Mg, Fe) bonds and/or to the combinations of OH librations and lattice modes [39, 40]. The band at about 609 cm^{-1} was assigned to the Fe–O stretching vibration of the Fe–O tetrahedron when sample was calcined at 400 °C [41]. The absorption band of the samples obtained above 200 °C, which appeared at about 3,400 cm^{-1}, was attributed to the adsorption of water from air.

XRD and SEM analysis of $Mn_{0.5}Mg_{0.5}Fe_2(C_2O_4)_3{\cdot}5H_2O$ and its calcined samples

Figure 3 shows the XRD patterns of $Mn_{0.5}Mg_{0.5}Fe_2(C_2O_4)_3{\cdot}5H_2O$ dried at 75 °C and the products resulting from calcination at different temperatures in air for 1 h.

From Fig. 3 characteristic diffraction peaks of crystalline compound from the precursor were observed, which indicated that $Mn_{0.5}Mg_{0.5}Fe_2(C_2O_4)_3{\cdot}5H_2O$ obtained at 75 °C was a crystal with higher crystallinity. The diffraction peaks in the pattern can be indexed to be in agreement with the orthorhombic $FeC_2O_4{\cdot}2H_2O$ from PDF card 23-0293, with space group *I*2/a(15). No diffraction peaks of manganese and magnesium oxalates, such as MnC_2O_4, $MnC_2O_4{\cdot}xH_2O$, MgC_2O_4, and $MgC_2O_4{\cdot}xH_2O$, were observed, which implied that Mn^{2+} and Mg^{2+} ions entered lattice of $FeC_2O_4{\cdot}2H_2O$. MnC_2O_4, $MnC_2O_4{\cdot}xH_2O$, MgC_2O_4, and $MgC_2O_4{\cdot}xH_2O$ formed a solid solution with $FeC_2O_4{\cdot}2H_2O$.

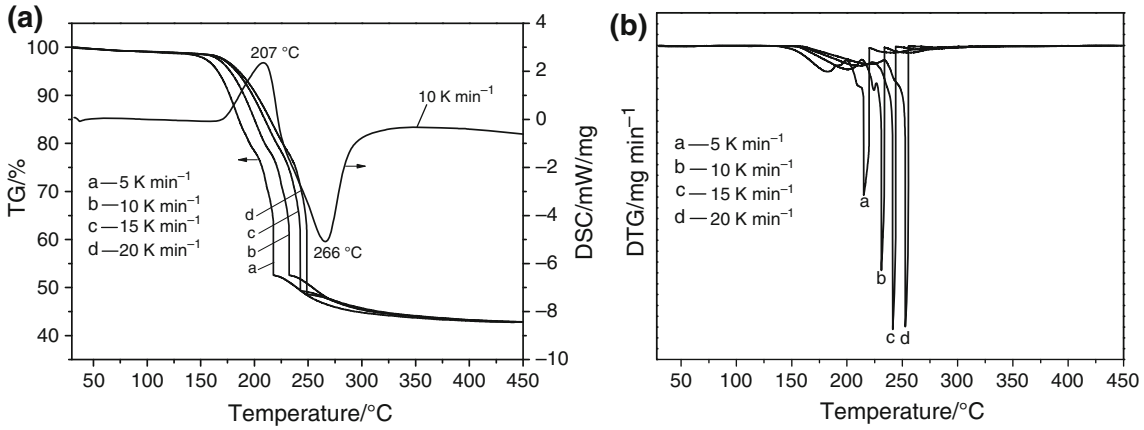

Fig. 1 TG/DTG/DSC curves of $Mn_{0.5}Mg_{0.5}Fe_2(C_2O_4)_3{\cdot}5H_2O$ at different heating rates in air

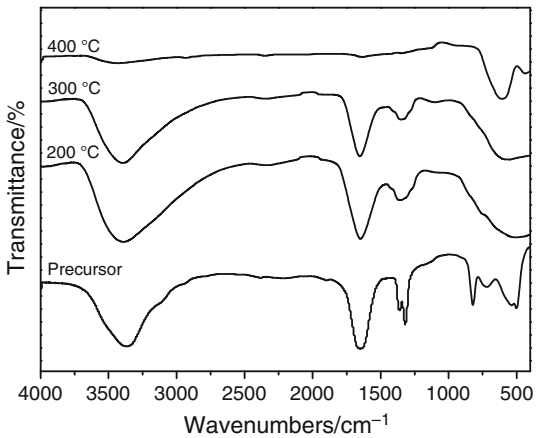

Fig. 2 FT-IR spectra of $Mn_{0.5}Mg_{0.5}Fe_2(C_2O_4)_3{\cdot}5H_2O$ and its calcined samples

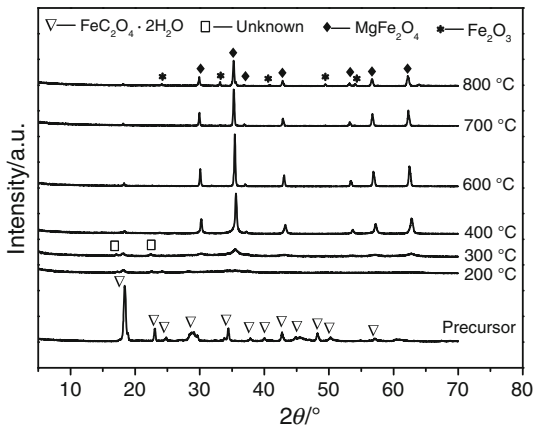

Fig. 3 XRD patterns of $Mn_{0.5}Mg_{0.5}Fe_2(C_2O_4)_3{\cdot}5H_2O$ and its calcined samples at different temperatures in air for 1 h

It is explained by the fact that Mn^{2+} ion (80 pm), Mg^{2+} ion (65 pm), and Fe^{2+} ion (76 pm) have same electric charge and similar ionic radius. When $Mn_{0.5}Mg_{0.5}Fe_2(C_2O_4)_3{\cdot}5H_2O$ was calcined at 300 °C for 1 h, a part of characteristic diffraction peaks of cubic $MgFe_2O_4$ were observed. When $Mn_{0.5}Mg_{0.5}Fe_2(C_2O_4)_3{\cdot}5H_2O$ was calcined at 400 °C, all the diffraction peaks in the pattern of sample were in agreement with that of cubic $MgFe_2O_4$, with space group *Fd*-3 *m*(227), lattice parameters: $a = b = c = 0.8387$ nm, $\alpha = \beta = \gamma = 90°$, density = 4.502 g cm^{-3}, from PDF card 36-0398. No diffraction peaks of crystalline $MnFe_2O_4$ were observed, which implied that $MnFe_2O_4$ and $MgFe_2O_4$ formed a solid solution. When sample was calcined at 800 °C, a part of characteristic diffraction peaks of rhombohedral Fe_2O_3 appeared, which implied that $Mn_{0.5}Mg_{0.5}Fe_2O_4$ was partly decomposed into Fe_2O_3.

According to the Scherrer formula [6]: $D = K\lambda/(\beta\cos\theta)$, where D is crystallite diameter, $K = 0.89$ (the Scherrer constant), $\lambda = 0.15406$ nm (wavelength of the X-ray used), β is the width of line at the half-maximum intensity, and θ is the corresponding angle. The resulting crystallite sizes of the products from calcining precursor at the temperatures of 400, 600, 700, and 800 °C in air for 1 h were 26, 41, 41, and 35 nm, respectively. Crystallite diameter of the product obtained at 800 °C was smaller than that of the samples obtained at 600 and 700 °C, which was attributed to $Mn_{0.5}Mg_{0.5}Fe_2O_4$ that was decomposed into Fe_2O_3 particles with smaller crystallite diameter at 800 °C. The crystallinity of cubic $Mn_{0.5}Mg_{0.5}Fe_2O_4$ can be evaluated via MDI Jade 5.0 software, the results showed that crystallinity of cubic $Mn_{0.5}Mg_{0.5}Fe_2O_4$ obtained at 400, 600, 700, and 800 °C were 98.73, 99.44, 99.51, and 92.59 %, respectively.

The morphologies and EDS spectrum of the calcined samples are shown in Fig. 4. From Fig. 4a it can be seen that the calcined sample obtained at 600 °C was composed of polyhedral particles, which contained particles having a distribution of small particles (100–200 nm) and large particles (200–300 nm). With the increase of calcination temperature, the crystallite in calcined sample was aggregated into larger grains further. Figure 4b and c show the

SEM micrographs of samples obtained at 700 and 800 °C, respectively. The calcined sample at 700 °C still kept polyhedral morphology, particles sizes are mainly between 300 and 400 nm. However, the calcined sample obtained at 800 °C became platelets grains with particle size of between 300 and 1,000 nm. The average crystallite sizes of the calcined samples determined by XRD were significantly smaller than the values determined by SEM. This was attributed to values observed by SEM technique that gave the size of the secondary particles, which were composed of several or many crystallites by soft reunion, and the X-ray line broadening analysis disclosed only the size of single crystallite. Figure 4d shows the EDS spectrum of product obtained at 700 °C in air, mole ratio of Mn:Mg:Fe was equal to 0.51:0.48:2.0, which was close to the value of the pre-design and synthesis.

Magnetic properties of the calcined samples

Figure 5 shows the hysteresis loops of $Mn_{0.5}Mg_{0.5}Fe_2O_4$ particles obtained at different calcination temperatures. From Fig. 5 it can be observed that specific saturation magnetizations of powders calcined at 400, 600, 700, and 800 °C for 1 h were 34.7, 46.2, 45.9, and 31.5 emu g^{-1}, respectively. That is, specific saturation magnetization of $Mn_{0.5}Mg_{0.5}Fe_2O_4$ powders increases between 400 and 600 °C with increasing calcination temperature at first, and then decreases. In other words, the larger the crystallite size of the particles, the larger is the specific saturation magnetizations. The larger *M*s values associated with larger crystallite sizes can be explained as follow: First, surface distortions due to the interaction of the transition metal ions with the oxygen atoms in the spinel lattice of $Mn_{0.5}Mg_{0.5}Fe_2O_4$ can reduce the net magnetic moment in the particle. When the calcination temperature increases, the crystallite size of particles increases, and surface distortions is reduced, so *M*s value increases with increasing calcination temperature. Second, the magnetocrystalline anisotropy of the particles is dependent on the crystallinity of $Mn_{0.5}Mg_{0.5}Fe_2O_4$. The higher calcination temperature, the larger is crystallinity of particles, which reduces magnetocrystalline anisotropy distortion, and increases magnetic moment within the particles of $Mn_{0.5}Mg_{0.5}Fe_2O_4$ [3, 11, 42]. Compared with magnetic properties of $MnFe_2O_4$ (500 °C, 9.5 emu g^{-1}; 700 °C, 41.5 emu g^{-1}) [5] and $MgFe_2O_4$ (600 °C, 30.4 emu g^{-1}; 700 °C, 35.7 emu g^{-1}) [6], it can be seen that $Mn_{0.5}Mg_{0.5}Fe_2O_4$ powders exhibits higher specific saturation magnetizations than $MnFe_2O_4$ and $MgFe_2O_4$

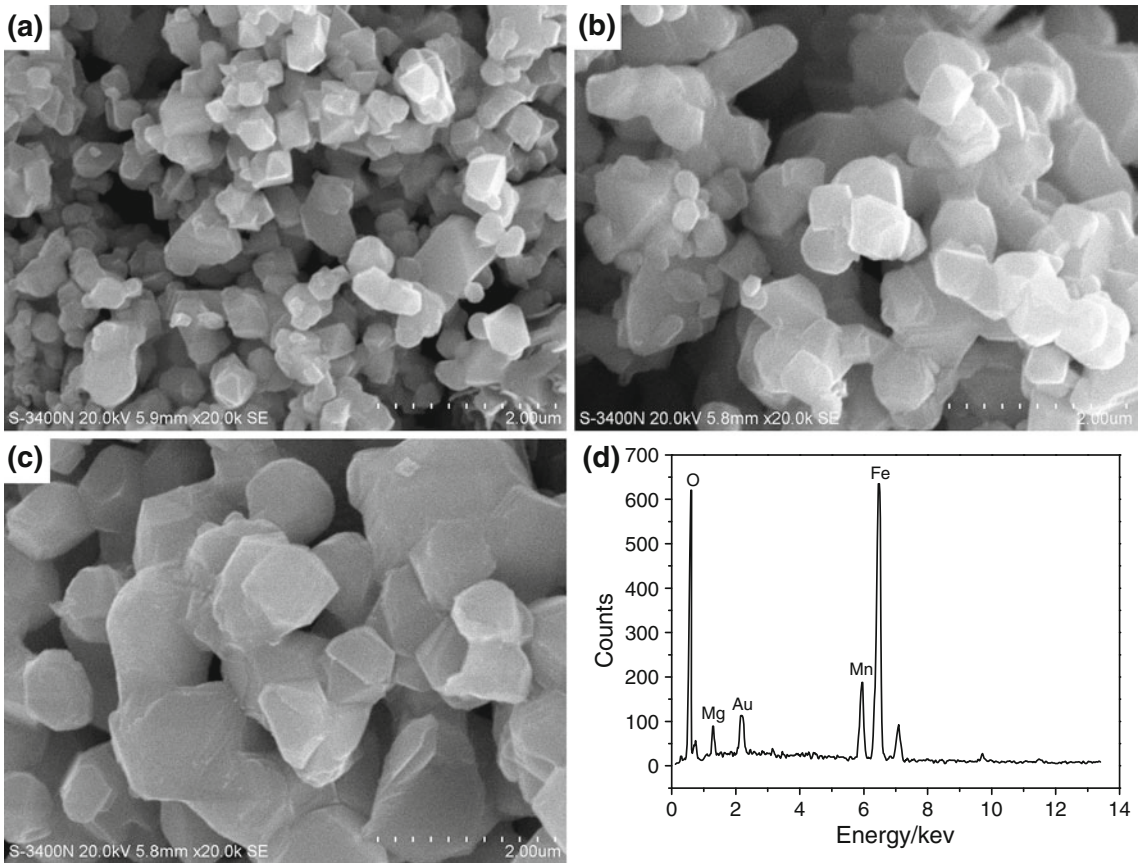

Fig. 4 SEM and EDS analysis of the calcined sample: SEM**: a** 600 °C, **b** 700 °C, and **c** 800 °C; EDS, **d** 700 °C

obtained at same calcination temperature, which implies that Mn^{2+} and Mg^{2+} ions in $Mn_{0.5}Mg_{0.5}Fe_2O_4$ have a synergistic effect in improving the specific saturation magnetization of $Mn_{0.5}Mg_{0.5}Fe_2O_4$. However, specific saturation magnetization of $Mn_{0.5}Mg_{0.5}Fe_2O_4$ powders decreases above 600 °C with increasing calcination temperature, which is attributed to $Mn_{0.5}Mg_{0.5}Fe_2O_4$ that was decomposed into Fe_2O_3 particles with weak magnetization above 700 °C.

Figure 6 shows effect of calcination temperature on coercivity and remanence of $Mn_{0.5}Mg_{0.5}Fe_2O_4$ powders. The results showed that coercivities (Hc) and remanences (Mr) of samples decreased with increasing calcination temperature between 400 and 700 °C.

Kinetics of thermal decomposition of $Mn_{0.5}Mg_{0.5}Fe_2(C_2O_4)_3{\cdot}5H_2O$

In accordance with TG/DTG/DSC, IR, and XRD analysis of $Mn_{0.5}Mg_{0.5}Fe_2(C_2O_4)_3{\cdot}5H_2O$ and its calcined products mentioned above, thermal decomposition of $Mn_{0.5}Mg_{0.5}Fe_2(C_2O_4)_3{\cdot}5H_2O$ below 450 °C in air consists of two steps, which can be expressed, respectively, as follows:

$$Mn_{0.5}Mg_{0.5}Fe_2(C_2O_4)_3{\cdot}5H_2O\ (cr) \rightarrow Mn_{0.5}Mg_{0.5}Fe_2(C_2O_4)_3(am) + 5H_2O\ (g) \quad (4)$$

$$Mn_{0.5}Mg_{0.5}Fe_2(C_2O_4)_3(am) + 2O_2(g) \rightarrow Mn_{0.5}Mg_{0.5}Fe_2O_4(c) + 6CO_2(g) \quad (5)$$

According to non-isothermal method, the basic data of α and T were collected from the TG curves of thermal decomposition of $Mn_{0.5}Mg_{0.5}Fe_2(C_2O_4)_3{\cdot}5H_2O$ at various heating rates (5, 10, 15, and 20 K min^{-1}). According to Eq. (1), the isoconversional calculation procedure of Starink equation was used. The corresponding Starink lines for different decomposition steps were obtained at different conversion degrees α and different heating rates β at first, and then reaction activation energy E_α can be obtained from linear slope ($-1.0008\ E_\alpha/R$). The results are shown in Table 1.

From Table 1, the activation energy changes for the step 1 with α are higher than 10 %, and that for the step 2 with α

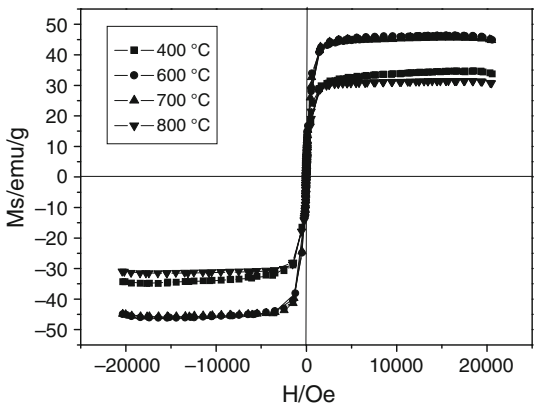

Fig. 5 Hysteresis loops for $Mn_{0.5}Mg_{0.5}Fe_2O_4$ samples obtained at different temperatures in air for 1 h

Table 1 Activation energies (E_α) and correlation coefficient (r^2) calculated by Starink method

Conversion degree α	Step 1		Step 2	
	E_α/kJ mol^{-1}	r^2	E_α/kJ mol^{-1}	r^2
0.1			80	0.9979
0.2	113	0.9688	82	0.9977
0.3	104	0.9845	81	0.9965
0.4	93	0.9905	85	9978
0.5	91	0.9933	87	0.9944
0.6	86	9950		
0.7	81	9962		
0.8	79	0.9971		
Av	92.4 ± 20.6	0.9893	83.0 ± 4.0	0.9969

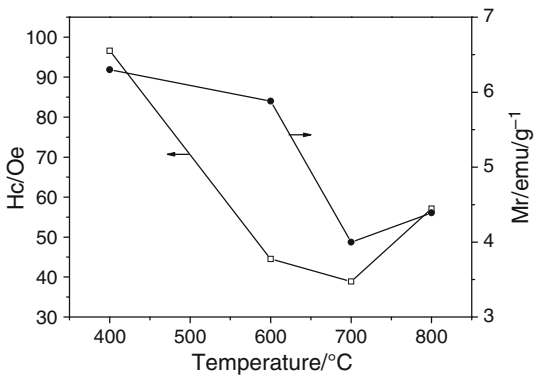

Fig. 6 Effect of calcination temperature on coercivity and remanence of samples

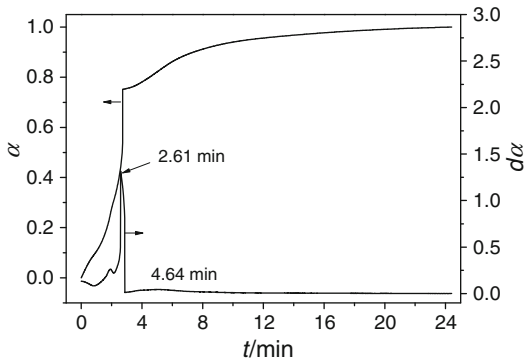

Fig. 7 Curves of α versus t and $d\alpha$ versus t at heating rate of 10 K min^{-1}

are lower than 10 %, so that we draw a conclusion that thermal decomposition of $Mn_{0.5}Mg_{0.5}Fe_2(C_2O_4)_3{\cdot}5H_2O$ for step 1 is multi-step reaction mechanisms. In other words, dehydration of $Mn_{0.5}Mg_{0.5}Fe_2(C_2O_4)_3{\cdot}5H_2O$ experiencing simple dehydration reactions of two or more steps; and reaction of $Mn_{0.5}Mg_{0.5}Fe_2(C_2O_4)_3$ with O_2 into $Mn_{0.5}Mg_{0.5}Fe_2O_4$ is simple reaction mechanisms [43–45]. The activation energy of the step 1 is higher than that of the step 2, which implies that the step 1 of the thermal decomposition of $Mn_{0.5}Mg_{0.5}Fe_2(C_2O_4)_3{\cdot}5H_2O$ may be interpreted as a ''slow'' stage, while step 2 may be interpreted as ''fast'' stage.

Figure 7 shows the curves of α versus t and $d\alpha$ versus t for step 2. From Fig. 7 it can be seen that step 2 consists of two models, that is, accelerating model between 0.0 and 2.71 min, and sigmoidal model between 2.71 and 24.5 min [31]. In accelerating model, rate increases continuously with increasing the extent of conversion and reaches its maximum at the end of the process, the result shows that rate of the accelerating stage reaches its maximum at 2.61 min. In sigmoidal model (sometimes also called autocatalytic), initial and final stages demonstrate the accelerating and decelerating behavior, respectively, so that the process rate reaches its maximum at some values of the extent of conversion, the result shows that rate for sigmoidal model reaches its maximum at about 4.64 min.

The appropriate temperatures corresponding to conversions for $\beta = 5$, 10, 15, and 20 K min^{-1} were determined at first and then conversions corresponding to an appropriate temperature for $\beta = 5$, 10, 15, and 20 K min^{-1} were put into 31 types of mechanism functions [34]. The slope k, correlation coefficient r^2, and intercept B of linear regression of ln $g(\alpha)$ versus ln β were obtained. The two mechanism functions of better correlation coefficient r^2 were determined to be probable mechanism functions at first, and then several temperatures were randomly chosen to calculate the slope k, correlation coefficient r^2, and intercept B of the two probable mechanism functions by the same method. Mechanism function, in which the value of k was closest to -1.00000 and the correlation coefficient r^2 was higher, was chosen as mechanism function of thermal decomposition of $Mn_{0.5}Mg_{0.5}Fe_2(C_2O_4)_3{\cdot}5H_2O$. The results showed that probable mechanism function integral form of thermal decomposition of $Mn_{0.5}Mg_{0.5}Fe_2(C_2O_4)_3{\cdot}5H_2O$ for step 2 was determined to be $g(\alpha) = [-\ln(1-\alpha)]^{1/3}$. Rate-determining mechanism for step 2 was assumed to be random nucleation.

The pre-exponential factor was obtained from Eq. (3), inserting the most probable mechanism function $g(\alpha)$, β, E_α, R, and T_{max} values. The results showed that the pre-exponential factor of thermal decomposition of $Mn_{0.5}Mg_{0.5}Fe_2(C_2O_4)_3{\cdot}5H_2O$ for steps 2 was determined to be $A = 3.03 \times 10^6$ s^{-1}.

Conclusions

We have successfully synthesized spinel $Mn_{0.5}Mg_{0.5}Fe_2O_4$ via calcining $Mn_{0.5}Mg_{0.5}Fe_2(C_2O_4)_3{\cdot}5H_2O$ in air. XRD analysis showed that precursor was a solid solution containing $MFe_2(C_2O_4)_3{\cdot}5H_2O$ (M=Mn, and Mg). $Mn_{0.5}Mg_{0.5}Fe_2O_4$ with cubic structure was obtained when the precursor was calcined above 400 °C in air for 1 h. Magnetic characterization indicated that the specific saturation magnetization of $Mn_{0.5}Mg_{0.5}Fe_2O_4$ obtained at 600 °C was 46.2 emu g^{-1}. Mn^{2+} and Mg^{2+} ions in $Mn_{0.5}Mg_{0.5}Fe_2O_4$ have a synergistic effect in improving the specific saturation magnetization of $Mn_{0.5}Mg_{0.5}Fe_2O_4$. The thermal decomposition of $Mn_{0.5}Mg_{0.5}Fe_2(C_2O_4)_3{\cdot}5H_2O$ in air in the range of ambient temperature to 450 °C experienced two steps which involved, at first, the dehydration of five water molecules, and then decomposition of $Mn_{0.5}Mg_{0.5}Fe_2(C_2O_4)_3$ into spinel $Mn_{0.5}Mg_{0.5}Fe_2O_4$ in air. Crystalline $Mn_{0.5}Mg_{0.5}Fe_2O_4$ can be obtained at lower calcination temperature, which was attributed to Mn^{2+}, Mg^{2+}, and Fe^{2+} oxalates that have similar lower decomposition temperature, and ultra-fine the oxide particles with high activity can be easily in situ self-assembled into crystalline $Mn_{0.5}Mg_{0.5}Fe_2O_4$. The kinetics of the thermal decomposition of $Mn_{0.5}Mg_{0.5}Fe_2(C_2O_4)_3{\cdot}5H_2O$ was studied using TG/DTG/DSC technique. The values of the activation energies associated with the thermal decomposition of $Mn_{0.5}Mg_{0.5}Fe_2(C_2O_4)_3{\cdot}5H_2O$ were determined to be 92.4 ± 20.6 and 83.0 ± 4.0 kJ mol^{-1} for the first and second thermal decomposition steps, respectively.

Acknowledgements This study was financially supported by the National Nature Science Foundation of China (Grant no. 21161002) and the Guangxi Nature Science Foundation of China (Grant no. 2011GXNSFA018036).

References

1. Marinca TF, Chicinas I, Isnard O. Influence of the heat treatment conditions on the formation of $CuFe_2O_4$ from mechanical milled precursors oxides. J Therm Anal Calorim. 2012;110:301–7.
2. Gabal MA, Ahmed MA. structural, electrical and magnetic properties of copper-cadmium ferrites prepared from metal oxalates. J Mater Sci. 2005;40:387–98.
3. Wu WW, Li YN, Zhou KW, Wu XH, Liao S, Wang Q. Nanocrystalline $Zn_{0.5}Ni_{0.5}Fe_2O_4$: preparation and kinetics of thermal process of precursor. J Therm Anal Calorim. 2012;110:1143–51.
4. Sun ZP, Liu L, Jia DZ, Pan WY. Simple synthesis of $CuFe_2O_4$ nanoparticles as gas-sensing materials. Sens Actuators B. 2007;125:144–8.
5. Li JJ, Yuan HM, Li GD, Liu YJ, Leng JS. Cation distribution dependence of magnetic properties of sol–gel prepared $MnFe_2O_4$ spinel ferrite nanoparticles. J Magn Magn Mater. 2010;322:3396–400.

6. Wu XH, Wu WW, Zhou KW, Cui XM, Liao S. Products and non-isothermal kinetics of thermal decomposition of $MgFe_2(C_2O_4)_3 \cdot 6H_2O$. J Therm Anal Calorim. 2012;110:781–7.
7. Li FS, Wang HB, Wang L, Wang JB. Magnetic properties of $ZnFe_2O_4$ nanoparticles produced by a low-temperature solid-state reaction method. J Magn Magn Mater. 2007;309:295–9.
8. Wu WW. C, Wu XH, Li YN, Liao S. Magnetic properties and crystallization kinetics of $Zn_{0.5}Ni_{0.5}Fe_2O_4$. Rare Met. 2011;30:621–6.
9. Satyanarayana L, Madhusudan Reddy K, Manorama SV. Nanosized spinel $NiFe_2O_4$: a novel material for the detection of liquefied petroleum gas in air. Mater Chem Phys. 2003;82:21–6.
10. Zhang K, Holloway T, Pradhan AK. Magnetic behavior of nanocrystalline $CoFe_2O_4$. J Magn Magn Mater. 2011;323:1616–22.
11. Wu WW, Cai JC, Wu XH, Liao S, Huang AG. $Co_{0.35}Mn_{0.65}Fe_2O_4$ magnetic particles: preparation and kinetics research of thermal process of the precursor. Powder Technol. 2012;215–216:200–5.
12. John Berchmans L, Karthikeyan R, Helan M, Berchmans Sheela, Ŝepelak V, Becker KD. Mechanochemical synthesis and electrochemical characterization of nano crystalline calcium ferrite. Catal Lett. 2011;141:1451–7.
13. Maqsood A, Faraz A. Synthesis, structural, electrical and magnetic characterization of $Mn_{0.5}Mg_{0.5-x}Ni_xFe_2O_4$ spinel Nanoferrites. J Supercond Nov Magn. 2011. doi:10.1007/s10948-011-1343-x.
14. Huang JW, Su P, Wu WW, Li YN, Wu XH, Liao S. Preparation of magnetic $Cu_{0.5}Mg_{0.5}Fe_2O_4$ nanoparticles and kinetics of thermal process of precursor. J Supercond Nov Magn. 2012;25:1971–7.
15. Wang WW. Microwave-induced polyol-process synthesis of $M^{II}Fe_2O_4$ (M = Mn, Co) nanoparticles and magnetic property. Mater Chem Phys. 2008;108:227–31.
16. Tromsdorf UI, Bigall NC, Kaul MG, Bruns OT, Nikolic MS, Mollwitz B, Sperling RA, Reimer R, Hohenberg H, Parak WJ, Förster S, Beisiegel U, Adam G, Weller H. Size and surface effects on the MRI, relaxivity of manganese ferrite nanoparticle contrast agents. Nano Lett. 2007;7:2422–7.
17. Liu XM, Yang G, Fu SY. mass synthesis of manocrystalline spinel ferrites by a polymer-pyrolysis route. Mater Sci Eng C. 2007;27:750–5.
18. Zhen L, He K, Xu CY, Shao WZ. Synthesis and characterization of single-crystalline $MnFe_2O_4$ nanorods via a surfactant-free hydrothermal route. J Magn Magn Mater. 2008;320:2672–5.
19. Wang J, Chen QW, Hou BY, Peng ZM. Synthesis and magnetic properties of single-crystals of $MnFe_2O_4$ nanorods. Eur J Inorg Chem. 2004;35:1165–8.
20. Ju YW, Park JH, Jung HR, Cho SJ, Lee WJ. Electrospun $MnFe_2O_4$ nanofibers: preparation and morphology. Compos Sci Technol. 2008;68:1704–9.
21. Zhang DE, Zhang XJ, Ni XM, Song JM, Zheng HG. Low-temperature fabrication of $MnFe_2O_4$ octahedrons: magnetic and electrochemical properties. Chem Phys Lett. 2006;426:120–3.
22. Iyer R, Desai R, Upadhyay RV. Low temperature synthesis of nanosized $Mn_{1-x}Zn_xFe_2O_4$ ferrites and their characterizations. Bull Mater Sci. 2009;32:141–7.
23. Faraz A, Saqib M, Ahmad NM, Fazal-ur-Rehman, Maqsood A, Usman M, Mumtaz A, Hassan MA. Synthesis, structural, and magnetic characterization of $Mn_{1-x}Ni_xFe_2O_4$ spinel nanoferrites. J Supercond Nov Magn. 2011. doi: 10.1007/s10948-011-1212-7.
24. Sharma SK, Ravi Kumar, Siva Kumar VV, Knobel M, Reddy VR, Gupta A, Singh M. Role of electronic energy loss on the magnetic properties of $Mg_{0.95}Mn_{0.05}Fe_2O_4$ nanoparticles. Nucl Instrum Methods Phys Res B. 2006;248:37–41.
25. Mansour SF, Elkestawy MA. A comparative study of electric properties of nano-structured and bulk Mn–Mg spinel ferrite. Ceram Int. 2011;37:1175–80.
26. Mansour SF. Structural and magnetic investigations of sub-nano Mn–Mg ferrite prepared by wet method. J Magn Magn Mater. 2011;323:1735–40.
27. Okasha N. Enhancement of magnetization of Mg–Mn nanoferrite by γ-irradiation. J Alloys Compd. 2010;490:307–10.
28. Maqsood A, Faraz A. Synthesis, structural, electrical and magnetic characterization of $Mn_{0.5}Mg_{0.5-x}Ni_xFe_2O_4$ spinel nanoferrites. J Supercond Nov Magn. 2012;25:1025–33.
29. Msomi JZ, Moyo T, Abdallah HMI. Magnetic properties of $Mg_xMn_{1-x}Fe_2O_4$ nanoferrites. J Supercond Nov Magn. 2012. doi:10.1007/s10948-011-1235-0.
30. Starink MJ. The determination of activation energy from linear heating rate experiments: a comparison of the accuracy of isoconversion methods. Thermochim Acta. 2003;404:163–76.
31. Vyazovkin S, Burnham AK, Criado JM, Pérez-Maqueda LA, Popescu C, Sbirrazzuoli N. ICTAC Kinetics Committee recommendations for performing kinetic computations on thermal analysis data. Thermochim Acta. 2011;520:1–19.
32. Vlaev L, Nedelchev N, Gyurova K, Zagorcheva M. A comparative study of non-isothermal kinetics of decomposition of calcium oxalate monohydrate. J Anal Appl Pyrol. 2008;81:253–62.
33. Liqing L, Donghua C. Application of iso-temperature method of multiple rate to kinetic analysis: Dehydration for calcium oxalate monohydrate. J Therm Anal Calorim. 2004;78:283–93.
34. Jiang HY, Wang JG, Wu SQ, Wang BS, Wang ZZ. Pyrolysis kinetics of phenol–formaldehyde resin by non-isothermal thermogravimetry. Carbon. 2010;48:352–8.
35. Wu XH, Wu WW, Cui XM, Liao S. Preparation of nanocrystalline $BiFeO_3$ via a simple and novel method and its kinetics of crystallization. J Therm Anal Calorim. 2012;107:625–32.
36. Boonchom B, Danvirutai C, Youngme S, Maensiri S. Simple synthesis, magnetic properties, and nonisothermal decomposition kinetics of $Fe(H_2PO_4)_2 \cdot 2H_2O$. Ind Eng Chem Res. 2008;47:7642–7.
37. Deb N. Solid-state thermal decomposition of heterobimetallic oxalate coordination compounds, zinc(II) tetraaquatris (oxalato) lanthanate(III)hexahydrate and cadmium(II) heptaaquatris(oxalato)lanthanate(III)tetrahydrate. J Therm Anal Calorim. 2012. http://dx.doi.org/10.1007/s10973-012-2437-9.
38. Deb N. Some heterobimetallic oxalate coordination precursors of lanthanum(III) of the type, $M_3[La(C_2O_4)_3(H_2O)_m]_2 \cdot nH_2O$ (M = Mn(II), Co(II), Ni(II) and Cu(II)). J Thermal Anal Calorim. 2012;107:561–71.
39. Donia AM. Synthesis, identification and thermal analysis of coprecipitates of silver-(cobalt, nickel, copper and zinc) oxalate. Polyhedron. 1997;16:3013–31.
40. Goel SP, Mehrotra PN. IR and thermal studies on lithium oxomolybdenum (VI) oxalate. J Therm Anal. 1985;30:145–51.
41. Berbenni V, Milanese C, Bruni G, Girella A, Marini A. Synthesis of $YFeO_3$ by thermal decomposition of mechanically activated mixtures $Y(CH_3COO)_3 \cdot 4H_2O$–$FeC_2O_4 \cdot 2H_2O$. Thermochim Acta. 2011;521:218–23.
42. Jiang CT, Liu RJ, Shen XQ, Zhu L, Song FZ. $Ni_{0.5}Zn_{0.5}Fe_2O_4$ nanoparticles and their magnetic properties and adsorption of bovine serum albumin. Powder Technol. 2011;211:90–4.
43. Budrugeac P, Muşat V, Segal E. Non-isothermal kinetic study on the decomposition of Zn acetate-based sol-gel precursor. J Therm Anal Calorim. 2007;88:699–702.
44. Chaiyo N, Muanghlua R, Niemcharoen S, Boonchom B, Seeharaj P, Vittayakorn N. Non-isothermal kinetics of the thermal decomposition of sodium oxalate $Na_2C_2O_4$. J Therm Anal Calorim. 2012;107:1023–9.
45. Huang JW, Su P, Wu WW, Li YN, Wu XH, Tao L. Preparation of nanocrystalline $BiFeO_3$ and kinetics of thermal process of precursor. J Therm Anal Calorim. 2012;. doi:10.1007/s10973-012-2524-y.